

# Nondestructive evaluation of cork enclosures using terahertz/millimeter wave spectroscopy and imaging

Yew Li Hor,<sup>1</sup> John F. Federici,<sup>1,\*</sup> and Robert L. Wample<sup>2</sup>

<sup>1</sup>Department of Physics, New Jersey Institute of Technology, Newark, New Jersey 07102, USA

<sup>2</sup>Department of Viticulture and Enology, California State University–Fresno, Fresno, California 93740, USA

\*Corresponding author: federici@adm.njit.edu

Received 19 September 2007; accepted 12 October 2007;  
posted 30 October 2007 (Doc. ID 87644); published 20 December 2007

Natural cork enclosures, due to their cell structure, composition, and low moisture are fairly transparent to terahertz (THz) and millimeter waves enabling nondestructive evaluation of the cork's surface and interior. It is shown that the attenuation coefficient of the defect-free cork can be modeled with a Mie scattering model in the weakly scattering limit. Contrast in the THz images is a result of enhanced scattering of THz radiation by defects or voids as well as variations in the cork cell structure. The presence of voids, defects, and changes in grain structure can be determined with roughly 100–300  $\mu\text{m}$  resolution. © 2008 Optical Society of America

OCIS codes: 110.6795, 120.4290, 300.6270.

## 1. Introduction

Natural cork is acquired from the Cork Oak (*Quercus suber*) predominately in Portugal and other countries surrounding the Mediterranean Sea. It is utilized in a variety of products including cork stoppers for wine and other beverages. As an enclosure for liquids, it has the desirable properties of being impermeable to liquids and gases, as well as compressible. The quality of cork enclosures is determined by the presence and size of defects, voids, or cracks. Methods of non-destructive evaluation (NDE) of corks include visible inspection of visible cracks and defects either by human experts or camera systems [1], chemical analysis (including cork soaks) for the presence of trichloroanisole (TCA) [2–4], and x-ray tomography [5].

In this paper, we examine the prospects of using terahertz (THz) and millimeter wave (MMW) spectroscopy and imaging as a NDE tool of natural cork enclosures. The potential of THz spectroscopy and imaging for NDE of materials such as space shuttle foam [6,7], moisture content in grain [8,9] and leaves [10,11], wood [12], pharmaceuticals [13], liquids [14], and explosives [15,16] is well documented. The key attribute of THz non-NDE is the ability of THz radi-

ation to propagate through paper, plastic, and other nonmetallic containers. In the case of natural cork, the large volume of gases and relatively low humidity ( $\sim 7\%$ ) enclosed by the cork cells enables the material to be compressible, yet exhibit fairly high THz transmission.

The interaction of THz radiation with materials depends in part on the material's phase: solid, liquid, or gas [17]. For gas-phase molecules, rotational and vibrational states typically occupy the THz region. Molecules that are polar, such as water vapor, exhibit many spectral lines due to their strong interaction with the THz electric field. Nonpolar molecules interact very little and are therefore transparent. For liquids, the rotational and vibrational excitations are strongly damped by the proximity of neighboring molecules. They are highly absorbing over a broad range of THz frequencies, thus generally yielding broad and continuum THz spectra. The Debye model seems to describe the THz experimental data of pure liquids very well and describes binary liquids fairly well with some modifications [18]. This model assumes that the molecule exhibits diffusionlike rotational motion characterized by a reorientational time constant  $\tau$ . In the case of intermolecular dynamics occurring on different time scales, multi-Debye fits may be used [18]. As described in our previous work, the THz absorption spectra of some crystalline solids

such as trichloroanisole (TCA) [19] results from an internal rotor. The rotors correspond to rotation about various axes in the molecule. In the case of TCA, one axis corresponds to the C—O bond where the hydrogens are effectively circling resulting in a symmetric three-fold barrier, while the other is the CH<sub>3</sub>O—C—benzene axis. The absorption in other crystals such as cyclotrimethylene trinitramine (RDX) [20] results from large-scale vibrational motion of the crystal structure.

The compound 2,4,6-TCA may participate in contamination of many foods and beverages, e.g., the muddy flavor in drinking water [21,22], sake, rice [23], and raisins [24]. 2,4,6-TCA is also thought to be the main compound responsible for cork taint in wine [25,26]. Also, 2,4,6-TCA has been recognized as an important indoor pollutant for its musty odors [27]. A small amount of 2,4,6-TCA can badly contaminate foods, beverages, and the environment. The consumer rejection threshold (CRT) of wine, for example, is 3.1 parts per 10<sup>12</sup> (ppt) [28], while the perceptible indoor air pollutant concentration is in the range of 5–10 ppt [27]. In our studies using THz time-domain spectroscopy (THz-TDS), we identified several spectral peaks in the absorbance spectra of 2,3,4-TCA, 2,4,6-TCA, and 2,5,6-TCA over the frequency range from 0.1 to 2 THz. Significant peaks were observed at 0.6, 0.95, and 1.2 THz for 2,4,6-TCA, 0.7 THz for 2,3,4-TCA, and 0.92 THz for 2,3,6-TCA. The observed absorption coefficients for TCA are not sufficiently strong enough to enable direct detection of TCA in cork enclosures at the sensitivity levels required for the CRT of 3.1 ppt.

In this paper, we detail the interaction of THz/MMW radiation with cork and emphasize the use of THz/MMW imaging and spectroscopy for a NDE of cork quality. Since the cork cells contain mostly gas, they are fairly transparent to THz radiation particularly in the MMW and low frequency THz range. Position dependent scattering of radiation allows one to image voids and defects in the internal structure. In Section 2, the sample preparation and experimental setup is detailed. Results, THz images, and analysis are described in Section 3. Comparison of THz, visible inspection, and x-ray tomography are compared in Section 4. Conclusions of this work are summarized in Section 5.

## 2. Experimental Setup

Natural cork samples are acquired from a variety of bottled wine varieties. Samples are dried in ambient air for several days. Samples roughly 4 mm thick were cut from the end of the cork that was not in contact with the wine. As a control, samples of cork that had not been used in the bottling process are also tested.

A T-Ray 2000 spectroscopy system (Picometrix, Inc.) is used in the transmission mode to measure the THz time-domain waveform. Details of the THz time-domain method may be found in [29]. A pair of silicon lenses (3 in. focal length) focuses the THz radiation to

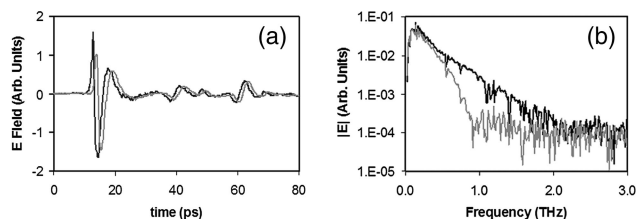


Fig. 1. (a) Measured THz time-domain waveform (gray) through a 4.4 mm thick cork sample. The reference waveform (black) is taken with the sample removed. (b) Corresponding amplitude as a function of frequency after Fourier transforming the time-domain data. Sharp structures near 0.57, 0.7, and 1.1 THz and other frequencies in the reference waveform are artifacts of absorption by water vapor in the atmosphere.

a spot at which the sample is placed. The imaging system consists of a pair of computer controlled linear translation stages (1  $\mu$ m resolution). The THz images are acquired by recording the THz transmitted pulse at each sample position. Typical THz time-domain waveforms are shown in Fig. 1. Spectral information as a function of frequency, both phase and amplitude, is acquired through a Fourier transform of the time-domain data.

As shown in Fig. 1, the slight time shift in the arrival of the peak of the pulse is indicative of the cork's real index of refraction. Typical values are between 1.07 and 1.1. In examining the magnitude of the THz electric field as a function of frequency, it is clear from the reference data that the THz amplitude approaches the noise limit of the THz system at approximately 2 THz. After passing through the cork sample, data beyond  $\sim$ 0.95 THz is in the noise for this particular sample location. For the spectroscopic data presented in this paper, only data within the signal to noise of the system are plotted for clarity.

THz images are formed by measuring the full time-domain waveform within an 80 ps time window. The sample is mechanically scanned in two directions at the focal point of the THz to generate an image one pixel at a time. Typical step sizes are 100–500  $\mu$ m.

## 3. Results and Discussion

There are many methods for analyzing the THz waveforms and generating a THz image. For example, one can measure the total transmitted THz power, the transmitted power within a given frequency interval, the change in the arrival time of the THz pulse, etc. At each pixel in the THz image, the THz phase and amplitude is normalized to the phase and amplitude of the reference waveform. Figure 2 shows the corresponding absorbance

$$A(\nu) = -\ln(T(\nu)) = -\ln(|E_s(\nu)|/|E_r(\nu)|) = \mu L, \quad (1)$$

at one pixel, where  $T(\nu)$  is the frequency dependent transmission referenced to a THz spectra with the sample removed.  $|E_s|$  and  $|E_r|$  are the magnitudes of the THz electric fields for the sample and reference, respectfully.  $L$  is the thickness of the sample, and  $\mu$  is defined as the attenuation coefficient.

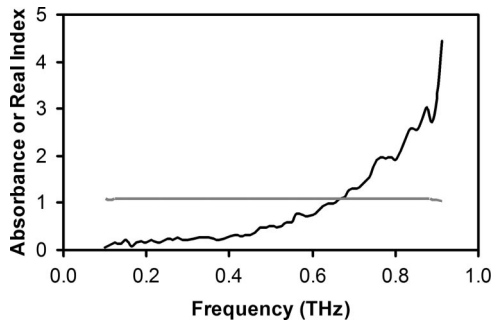


Fig. 2. Calculated frequency dependent absorbance (black) and real index of refraction (gray) for the time-domain waveforms of Fig. 1.

Figure 2 also shows the frequency dependence of the real index of refraction as calculated by

$$n_{\text{real}}(\nu) = \frac{(\phi_r(\nu) - \phi_s(\nu))c}{2\pi\nu L} + 1, \quad (2)$$

where  $\phi_s$  and  $\phi_r$  are the Fourier transformed frequency dependent phases of the sample and reference waveforms, respectively,  $c$  is the speed of light,  $L$  is the thickness of the sample, and  $\nu$  is the frequency. Note that the real index of refraction is essentially constant over the measured range.

The visible and typical THz images of cork samples are shown in Figs. 3–5. The THz images are formed by calculating the average transmitted power in the

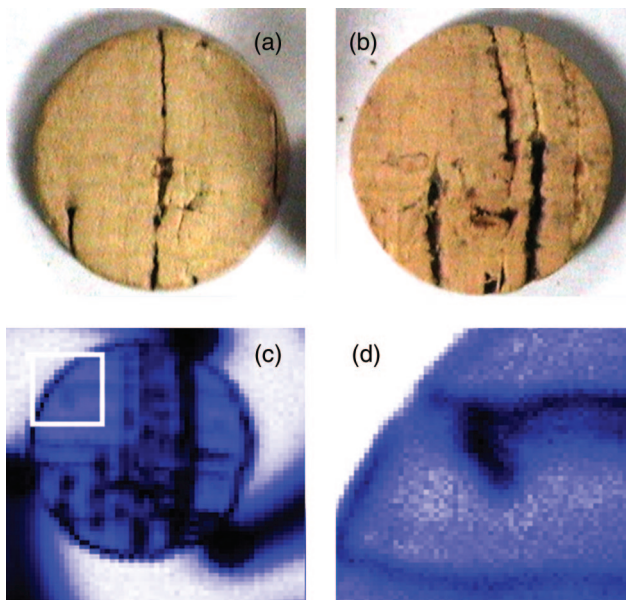


Fig. 3. (Color online) Front (a) and back visible (b) and 0.6–0.7 THz (c) image through a 4.4 mm cork sample. Each pixel is 500  $\mu\text{m}$ . The front of the cork corresponds to the end that nominally would be in contact with the wine and the portion of the back side that could be visibly inspected. The visible image of the back side image is reversed left to right for easier comparison to the THz image. The sample is oriented so that the grains of the cork are parallel to the bottom of the page. The image (0.9–1.0 THz transmission) of (d) is a high resolution (100  $\mu\text{m}$  pixel) image of the area outlined in white.

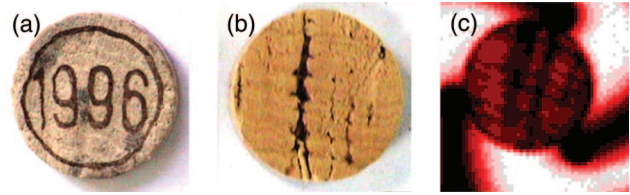


Fig. 4. (Color online) Front and back visible (left) and terahertz (right) images through a 4.35 mm (upper) sample from a different cork from Fig. 3. As with Fig. 3, note the presence of cracks, void, and cork grain that are visible in the terahertz image that otherwise would be overlooked in examining only the front visible image.

0.9–1.0 THz frequency band. The sample holder, which is made of aluminum, appears dark in the image since it blocks THz radiation. The sample is oriented so that the grain structure of the cork lies roughly parallel to the bottom of the page.

In comparing the visible and THz images, it is clear that the THz image shows the presence of the cork grain as well as the presence of defects and voids. In examining only the front visible image, one would be led to the false assumption that the cork sample of Fig. 3 is fairly uniform with only one large crack in the middle of the sample and a smaller one in the lower left corner. Likewise, in examining the front visible image of Fig. 4 one would be led to the false conclusion that the cork is defect free. However, the THz image shows the presence of three major cracks/voids in the first 4.35 mm of cork. Since the THz transmits through the cork and enables one to non-destructively evaluate the interior structure, the THz image shows the presence of a larger number of cracks and voids that would nominally be invisible if one were to simply visibly inspect the cork surfaces.

Figure 6 shows THz transmission images of the same cork in 0.1 THz bandwidths. The frequency range is 0.1–0.2 THz for the top left image and 0.9–1.0 THz for the bottom right image. As the THz frequency increases, the spatial resolution improves. This is expected since one would expect the spatial resolution to degrade with increasing THz wavelength (decreasing THz frequency) due to diffractive effects. It is also interesting to note that the contrast of the image appears to change as a function of frequency. For example, while all of the vertical cracks are visible in the 0.9–1.0 THz image, portions of those cracks are missing in the 0.5–0.6 THz images. Moreover, fairly high transmission regions, particu-

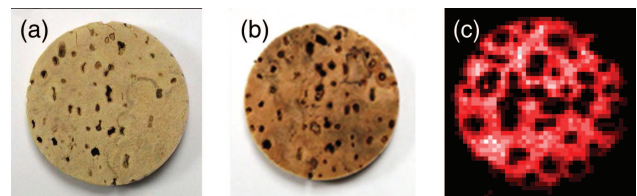


Fig. 5. (Color online) Front and back visible (left) and THz (right) image through a 4.02 mm sample. This sample shows the image of hole (bright spot) and cavities (dark spot) that are visible in the THz image.

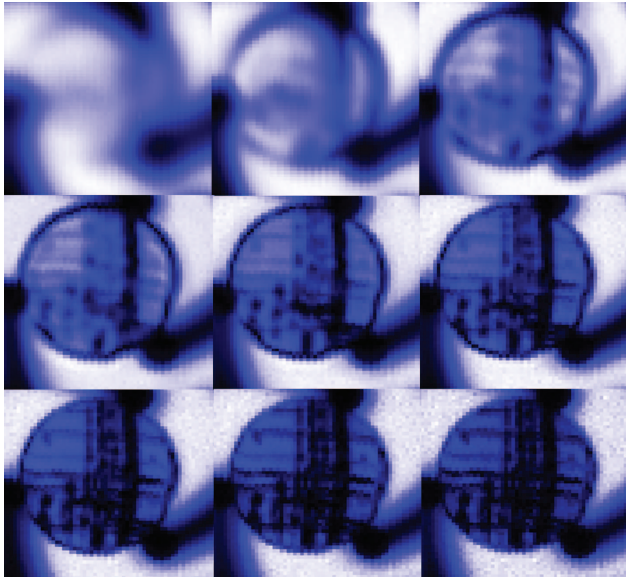


Fig. 6. (Color online) THz transmission images in 0.1 THz bandwidths from 0.1–0.2 THz through 0.9–1.0 THz (left to right, top to bottom progression). Note the improvement in spatial resolution with increasing THz frequency. Each pixel is 500  $\mu\text{m}$ .

larly in the upper left quarter of the sample, are prevalent in the THz images below 0.7 THz but are absent for THz images above 0.7 THz. As discussed below, the THz radiation interacts differently with the cracks, voids, and grains creating the contrast in the THz images.

To understand the differences in the darker features of Figs. 3 and 6, we examined the spectral shape of the absorbance at various positions of the sample. The presence of the large voids and cracks are characterized by spectral peaks in the absorbance as illustrated in Fig. 7. While the location of the spectral peak may vary between 0.3 and 0.5 THz at different

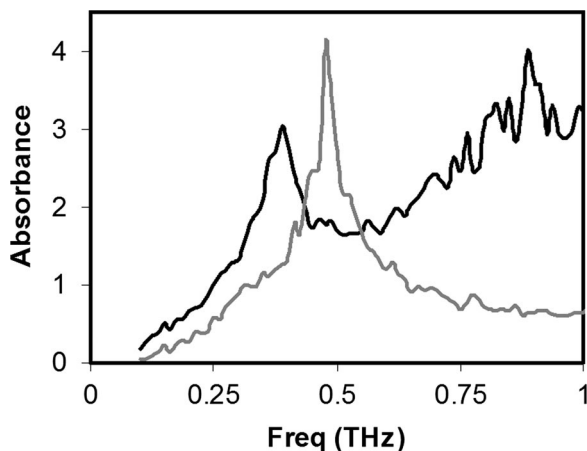


Fig. 7. Absorption spectra (black) from pixel position (x37, y42) of Fig. 3 corresponding to a large crack/void in the THz cork image. Note the presence of the sharp feature near 0.39 THz. Corresponding spectra (gray) from pixel position (x13, y51) corresponding to the edge of the cork. Note again the presence of an anomalous spectral peak near 0.47 THz.

positions of the cracks/void, the peak is always present. For the edge of the cork, the peak position varies between 0.4 and 0.6 THz depending on the location. We suspect that the absorbance peaks of Fig. 7 are an artifact of enhanced scattering of the THz radiation by the presence of boundaries or cracks/voids.

In examining locations on the sample for which there are no edges or voids or cracks, one observes in the THz images the presence of dark and clear bands parallel to the direction of the grain structure. The absorbance spectra at these locations typically do not exhibit any spectral peaks but rather an increasing absorbance with frequency that may be fit to a power law dependence,

$$A(\nu) = C\nu^m + B, \quad (3)$$

where  $A(\nu)$  is the frequency dependent absorbance,  $\nu$  is the THz frequency, and  $C$ ,  $B$ , and  $m$  are fit parameters. Within the same dark or light band, there is some variation in the extracted parameters, but the spectral shape of the absorbance is consistent within the same dark or light band.

To gauge the range of extracted parameters, the THz absorption spectra are analyzed for different light and dark grains. Table 1 summarizes the data for several different corks. The average and uncertainty of the values for the  $C$  or  $m$  coefficients are determined by the average and standard deviation for the set of ten measurements on each cork sample. In comparing grains from the same cork, both the  $C$  and  $m$  coefficients increase from light to dark grains. This increase is indicative of enhanced THz scattering in the dark grains.

THz images can also be generated based on the time delay in the arrival of the THz pulse or analogously the frequency dependent phase of the THz wave. While time-delay and phase THz images (not shown) show the presence of similar structures as the THz amplitude images, the contrast is considerably degraded. Since the arrival time is determined by the optical path length (i.e., the product of the real index of refraction and the physical thickness of the sample), one would expect the contrast in a time delay or phase image to be a result of either local variations in the thickness of the sample or variations in the real index of refraction. From THz phase images, we estimate that change in the optical path length between light and dark grains to be approximately 30  $\mu\text{m}$ . In comparison, the size of a cork cell is approximately 36–50  $\mu\text{m}$ . The fact that the time delay of the THz pulse through the sample is essentially independent of position further suggests that the contrast in the amplitude images is essentially due to scattering rather than an intrinsic absorption.

Since the size of the cork cells ( $\sim 36\text{--}50 \mu\text{m}$ ) are approaching the wavelength of the THz radiation (1 THz corresponds to a 300  $\mu\text{m}$  wavelength) as the THz frequency increases, this suggests that the frequency dependent absorbance can be modeled with

Table 1. Summary of Extracted Parameters from Power Law Dependence of Absorbance Spectra

Sample	Light Grain		Dark Grain		Cavity	
	<i>C</i>	<i>m</i>	<i>C</i>	<i>m</i>	<i>C</i>	<i>m</i>
Fig. 3	0.85 ± 0.13	1.46 ± 0.43	2.40 ± 0.82	2.33 ± 0.82	—	—
Fig. 4	1.37 ± 0.08	1.64 ± 0.39	2.09 ± 0.68	1.76 ± 0.43	—	—
Fig. 5	1.31 ± 0.48	1.11 ± 0.29	—	—	4.63 ± 0.54	1.33 ± 0.75

Mie scattering theory for regions of the cork, which are free of defects and voids. Our earlier work [15,30] on THz scattering and attenuation through powders showed that the THz absorbance by small particles can be modeled by Mie scattering theory. In particular, in the weakly scattering limit, Mie scattering produces a power law frequency dependent absorbance.

If the sample is assumed to consist of spherical scatterers [30], the attenuation coefficient [ $\mu$  in Eq. (1)] in Mie theory takes on the following form:

$$\mu_{th} = N \frac{c^2}{2\pi\nu^2} \sum_{m=1}^{\infty} (2m + 1) \text{Re}(a_m + b_m), \quad (4)$$

where  $N$  is the number of scattering centers per unit volume,  $c$  is the speed of light, and  $a_m$  and  $b_m$  are the coefficients in the infinite summation such that

$$a_m = \frac{\psi_m'(y)\psi_m(x) - n\psi_m(y)\psi_m'(x)}{\psi_m'(y)\zeta_m(x) - n\psi_m(y)\zeta_m'(x)},$$

$$b_m = \frac{n\psi_m'(y)\psi_m(x) - \psi_m(y)\psi_m'(x)}{n\psi_m'(y)\zeta_m(x) - \psi_m(y)\zeta_m'(x)},$$

where

$$\psi_m(z) = zj_m(z),$$

$$\zeta_m(z) = zh_m^{(2)}(z). \quad (5)$$

Here  $j_m(z)$  and  $h_m^{(2)}(z)$  are spherical Bessel functions of the first kind and third kind, respectively, when  $z$  can be either  $x = 2\pi\nu r/c$  or  $y = 2\pi\nu nr/c$ ,  $r$  is the radius of the spherical grain, and  $n$  is the frequency independent refractive index.

In applying this model to natural cork, we note that several approximations are assumed. For example, cork cells are not spherical, but rectangularly shaped. Moreover, the cork cell itself is not homogeneous, but rather a cell wall surrounding trapped gases. For the purposes of this simple model, we assume that the cork cell is uniform with a real index of refraction given by the THz spectroscopy measurements (~1.07–1.1).

Using a microscope to inspect the cork cells, we note that the cells are roughly 36  $\mu\text{m}$  in size, and exhibit a regular rectangularlike shape that is typical of cork cells. Using the Mie scattering model of Eqs. (4) and (5), we estimate the frequency dependence of the absorbance for particles with index of refraction

1.07, sample thickness 4.4 mm, and particle sizes of  $r = 18 \mu\text{m}$  corresponding roughly to the size of the cork cell.  $N$ , the number of particles per unit volume, is estimated based on the volume of a cork cell to be  $N \sim 2 \times 10^{13}$ . The estimated absorbance is shown in Fig. 8. Fitting these curves to a power law dependence yields fitting parameters from Eq. (3) of  $C = 1.837$ ,  $m = 1.91$  for 18  $\mu\text{m}$  particles. We note that these parameters are comparable to the parameters extracted from the THz absorbance data for Fig. 3.

To understand the origin of the contrast in dark and light THz grains, one needs to consider possible changes in the cell structure or density that could modify the efficiency of scattering. Typically during the spring, cork trees are growing more rapidly (spring wood), and the cork cells are larger. In comparison, the new cells that are formed during the summer growth are smaller (summer wood) and more densely packed. Moreover, as the tree grows radially and the diameter of the tree expands, the regular pattern of cells cannot be maintained. Consequently, a disruption in the regularity of the cell structure occurs leading to cracks, voids, or a change

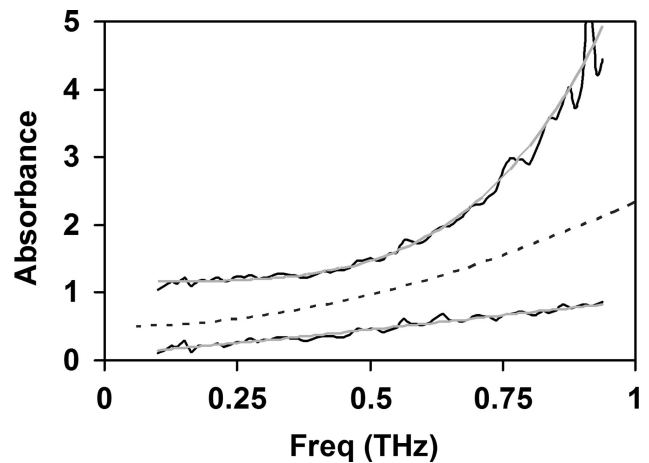


Fig. 8. Measured absorbance (upper black curve) from pixel position (x15, y34) of Fig. 3 (vertically offset by 1.0) corresponding to a dark grain in the cork THz image. Gray curve is a power law fit to the data using Eq. (3). Extracted parameters:  $C = 4.844$ ,  $m = 4.002$ ,  $B = 0.1636$ . Bottom curve is the absorbance spectra from pixel position (x14, y32) corresponding to a clear grain in the cork THz image. Extracted parameters:  $C = 0.7924$ ,  $m = 1.126$ ,  $B = 0.09013$ . The dashed curve (vertically offset by 0.5) is the predicted absorbance of 18  $\mu\text{m}$  radius particles. The index of refraction is 1.1, sample thickness 4.4 mm, and the number of particles per volume is  $2 \times 10^{13} \text{ m}^{-3}$ . Fitting these curves to a power law dependence yields fitting parameters from Eq. (3) of  $A = 1.837$ ,  $m = 1.91$ .

in grain structure. Either an increase in cell size or disruption in the grain structure could lead to increased THz scattering and explain the observed contrast in the THz images.

#### 4. Comparison of Natural Cork Nondestructive Evaluation Methods

In comparing THz imaging and spectroscopy as a nondestructive evaluation method of corks with the established methods of visible inspection of visible cracks and defects by human experts/camera systems [1] and x-ray tomography [5], it is clear that THz imaging has much of the same capabilities as well as some unique features. While human experts and camera systems can only inspect the surface of the cork, both THz imaging and x-ray tomography enable evaluation of the internal structure of the cork as well as the surface structure. The spatial resolution of the camera system reported in [1] images the end of a cork with approximately  $90 \times 90$  pixels. The THz images of the end of the cork are roughly  $45 \times 45$  pixels corresponding to 0.5 mm spatial resolution. The maximum resolution is determined by the step size of each pixel as well as the THz frequency. Since the spatial resolution of a free-space optical system is typically limited by diffractive effects to be on the order of the wavelength of light, one would expect that the resolution limit of 1 THz radiation would be on the order of 300  $\mu\text{m}$ . Therefore, halving the pixel step size to 250  $\mu\text{m}$  in the THz images would give approximately the same spatial resolution as the visible images of [1] but with the added advantage of probing the interior structure of the cork.

As described in [5], an x-ray transmission geometry does not produce good contrast x-ray images. The poor contrast results from the fact that the interaction between the x rays and cork is very weak so that there is very little loss of x-ray power going in through the natural cork cells and the voids. This is in contrast with the THz transmission imaging method for which there is a strong interaction between the THz radiation and the cork cell structure due to Mie scattering: the size of the cork cells is comparable to the wavelength of the probing radiation. THz radiation, as compared to x rays, is more efficiently scattered by the cells and voids implying that THz imaging is a much more sensitive method for imaging the internal structure of the cork.

The x-ray tomography technique of [5] measures scattered x rays by placing the x-ray receiver approximately perpendicular to the incoming direction of the probing x rays. Regions of high electron density more efficiently scatter the x rays resulting in contrast between the cork and voids. (It should be noted that THz tomography [31–33] has also been used to reconstruct 3D images of objects.) The x-ray beam is collimated to a diameter of roughly 1 mm and passed through the sample. Since the spatial resolution of the x-ray method will be limited to roughly 1 mm (as determined by the diameter of the probing x-ray beam), the spatial resolution of the THz system is inherently superior to that described in [5]. More-

over, a two-dimensional (2D) linear scan as well as a rotational scan is required to reconstruct the x-ray tomography images. Since THz radiation interacts much more strongly with the cork cell structure through Mie scattering, a simple transmission image requires only a 2D linear scan.

The contrast between mature cork and green cork (higher concentration of water or cytoplasmic liquid) is readily observable with the x-ray tomography method. THz transmission imaging, as well, should be able to distinguish mature from green cork. Since water and liquids in general highly reflect THz radiation, green cork should efficiently reflect/attenuate THz radiation compared to mature cork.

#### 5. Conclusion

THz spectroscopy and imaging is applied to nondestructive evaluation of natural cork. Using a time-domain THz spectroscopy and imaging system, THz transmission images are generated in the 0.1–2 THz range. The presence of voids, cracks, and defects in the cork are evident in the THz image due to enhanced scattering of THz radiation. Furthermore, the cork's grain structure can be imaged. Analysis of the spectral properties of the cork shows that the THz absorbance can be modeled by a power law. A simple application of Mie scattering in the low scattering region qualitatively fits the observed spectral properties. The contrast in the THz transmission through different grains is likely due to variations in the cell structure that occur during the seasonal growth of the cork tree.

Helpful discussions with K. Tandon, K. Fugelsang, R. M. Federici, and J. M. Joseph are gratefully acknowledged. Assistance by C. Prodan in acquiring microscopic images of the cork cell structure is gratefully acknowledged.

#### References

1. J. Chang, G. Han, J. M. Valverde, N. C. Griswold, J. F. Duque-Carrillo, and E. Sanchez-Sinencio, "Cork quality classification system using a unified image processing and fuzzy-neural network methodology," *IEEE Trans. Neural Netw.* **8**, 964–974 (1997).
2. R. Juanola, D. Subirà, V. Salvadó, J. A. Garcia Regueiro, and E. Anticó, "Evaluation of an extraction method in the determination of the 2,4,6-trichloroanisole content of tainted cork," *J. Chromatogr. A* **953**, 207–214 (2002).
3. E. Lizarraga, Á. Irigoyen, V. Belsue, and E. González-Peñas, "Determination of chloroanisole compounds in red wine by head-space solid-phase microextraction and gas chromatography-mass spectrometry," *J. Chromatogr. A* **1052**, 145–149 (2004).
4. E. Herve, S. Price, G. Burns, and P. Weber, presented at the ASEV Annual Meeting, Reno, Nevada, 2 July 1999. <http://www.corkqc.com/asev/asev2-2.htm>.
5. A. Brunetti, R. Cesareo, B. Golosio, P. Luciano, and A. Ruggero, "Cork quality estimation by using Compton tomography," *Nucl. Instrum. Methods Phys. Res. B* **196**, 161–168 (2002).
6. D. Zimdars, J. S. White, G. Stuk, A. Chernovsky, G. Fichter, and S. Williamson, "Large area terahertz imaging and non-destructive evaluation applications," *Insight-Non-Destruct. Test. Condition Monitor.* **48**, 537–539 (2006).
7. D. Zimdars, J. A. Valdmans, J. S. White, G. Stuk, W. P.

- Winfree, and E. I. Madaras, "Time domain terahertz detection of flaws within space shuttle sprayed on foam insulation," in *Conference on Lasers and Electro-Optics/(CLEO)*, Vol. 96 of OSA Trends in Optics and Photonics (Optical Society of America, 2004), paper CThN4. <http://www.opticsinfobase.org/abstract.cfm?id=104293>.
8. H. S. Chua, P. C. Upadhyaya, A. D. Haigh, J. Obradovic, A. A. P. Gibson, and E. H. Linfield, "Terahertz time-domain spectroscopy of wheat grain," in *Conference Digest of the 2004 Joint 29th International Conference on Infrared and Millimeter Waves and 12th International Conference on Terahertz Electronics* (IEEE, 2004), pp. 399–400.
  9. H. S. Chua, J. Obradovic, A. D. Haigh, P. C. Upadhyaya, O. Hirsch, D. Crawley, A. A. P. Gibson, and E. H. Linfield, "Terahertz time-domain spectroscopy of crushed wheat grain," in *2005 IEEE MTT-S International Microwave Symposium* (IEEE, 2005), p. 4.
  10. S. Hadjiloucas, L. S. Karatzas, and J. W. Bowen, "Measurements of leaf water content using terahertz radiation," *IEEE Trans. Microwave Theory Tech.* **47**, 142–149 (1999).
  11. S. Hadjiloucas, R. K. H. Galvao, and J. W. J. Bowen, "Analysis of spectroscopic measurements of leaf water content at terahertz frequencies using linear transforms," *J. Opt. Soc. Am. A* **19**, 2495–2509 (2002).
  12. M. Reid and R. Fedosejevs, "Terahertz birefringence and attenuation properties of wood and paper," *Appl. Opt.* **45**, 2766–2772 (2006).
  13. C. J. Strachan, T. Rades, D. A. Newnham, K. C. Gordon, M. Pepper, and P. F. Taday, "Using terahertz pulsed spectroscopy to study crystallinity of pharmaceutical materials," *Chem. Phys. Lett.* **390**, 20–24 (2004).
  14. D. S. Venables and C. A. Schmuttenmaer, "Spectroscopy and dynamics of mixtures of water with acetone, acetonitrile, and methanol," *J. Chem. Phys.* **113**, 11222–11236 (2000).
  15. J. F. Federici, B. Schulkin, F. Huang, D. Gary, R. Barat, F. Oliveira, and D. Zimdars, "THz imaging and sensing for security applications—explosives, weapons and drugs," *Semicond. Sci. Technol.* **20**, S266–S280 (2005).
  16. J. F. Federici, D. Gary, R. Barat, and Z.-H. Michalopoulou, "Detection of Explosives by Terahertz Imaging," in *Counter-Terrorism Detection Techniques of Explosives*, J. Yinon, ed. (Elsevier, 2007).
  17. F. C. Delucia, "Spectroscopy in the terahertz spectral region," in *Sensing with Terahertz Radiation*, D. Mittleman ed. (Springer, 2003).
  18. M. C. Beard, G. M. Turner, and C. A. Schmuttenmaer, "THz spectroscopy," *J. Phys. Chem B* **106**, 7146–7159 (2002).
  19. Y. L. Hor, H. C. Lim, J. F. Federici, E. Moore, and J. W. Bozzelli, "Terahertz spectroscopy of trichloroanisole," (submitted to *Chem. Phys. Lett.*).
  20. F. Huang, B. Schulkin, H. Altan, J. Federici, D. Gary, R. Barat, D. Zimdars, M. Chen, and D. Tanner, "Terahertz study of 1,3,5-trinitro-s-triazine by time-domain and Fourier transform infrared spectroscopy," *Appl. Phys. Lett.* **85**, 5535–5537 (2004).
  21. A. Nystrom, A. Grimvall, C. Krantz-Rulcker, R. Savenhed, and K. Akerstrand, "Water off-flavour caused by 2,4,6-trichloroanisole," *Water Sci. Technol.* **25**, 241–249 (1992).
  22. S. Karlsson, S. Kaugare, A. Grimvall, H. Boren, and R. Savenhed, "Formation of 2,4,6-trichlorophenol and 2,4,6-trichloroanisole during treatment and distribution of drinking water," *Water Sci. Technol.* **31**, 99–103 (1995).
  23. A. Miki, A. Isogai, H. Utsunomiya, and H. Iwata, "Identification of 2,4,6-trichloroanisole (TCA) causing a musty/muddy off-flavor in sake and its production in rice koji and moromi mash," *J. Biosci. Bioeng.* **100**, 178–183 (2005).
  24. L. H. Aung, J. L. Smilanick, P. V. Vail, P. L. Hartsell, and E. Gomez, "Investigations into the origin of chloroanisoles causing musty off-flavor of raisins," *J. Agric. Food Chem.* **44**, 3294–3296 (1996).
  25. C. Silva Pereira, J. J. Figueiredo Marques, and M. V. San Romao, "Cork taint in wine: scientific knowledge and public perception—a critical review," *Crit. Rev. Microbiol.* **26**, 147–162 (2000).
  26. A. P. Pollnitz, K. H. Pardon, D. Liacopoulos, G. K. Skouroumounis, and M. A. Sefton, "The analysis of 2,4,6-trichloroanisole and other chloroanisoles in tainted wines and corks," *Aust. J. Grape Win. Res.* **2**, 184–190 (1996).
  27. J. Gunschera, F. Fuhrmann, T. Salthammer, A. Schulze, and E. Uhde, "Formation and emission of chloroanisoles as indoor pollutants," *Environ. Sci. Pollut. Res.* **11**, 147–151 (2004).
  28. J. Prescott, L. Norris, M. Kunst, and S. Kim, "Estimating a consumer rejection threshold for cork taint in white wine," *Food Qual. Pref.* **16**, 345–349 (2005).
  29. D. Mittleman, "Terahertz imaging," in *Sensing with Terahertz Radiation*, D. Mittleman, ed. (Springer, 2003).
  30. A. Sengupta, A. Bandyopadhyay, J. F. Federici, R. B. Barat, D. E. Gary, M. Chen, and D. B. Tanner, "Effects of scattering on THz spectra of granular solids," *Int. J. Infrared Millim. Waves* (to be published).
  31. D. M. Mittleman, S. Hunsche, L. Boivin, and M. C. Nuss, "T-ray tomography," *Opt. Lett.* **22**, 904–906 (1997).
  32. T. Yasui, T. Yasuda, T. Araki, and E. Abraham, "Real-time two-dimensional terahertz tomography of moving objects," *Opt. Commun.* **267**, 128–136 (2006).
  33. H. Zhong, J. Xu, X. Xie, T. Yuan, R. Reightler, E. Madaras, and X.-C. Zhang, "Nondestructive defect identification with terahertz time-of-flight tomography," *IEEE Sens. J.* **5**, 203–208 (2005).